Journal of Power Sources 196 (2011) 1915–1919

Contents lists available at ScienceDirect

Journal of Power Sources

journal homepage: www.elsevier.com/locate/jpowsour

Short communication

Analysis of the three-dimensional microstructure of a solid-oxide fuel cell anode using nano X-ray tomography

Yong Guan[a,b,1], Wenjie Li[a,b,1], Yunhui Gong[c], Gang Liu[a,b], Xiaobo Zhang[a], Jie Chen[a,b], Jeff Gelb[d], Wenbing Yun[d], Ying Xiong[a,b], Yangchao Tian[a,b,*], Haiqian Wang[c,**]

[a] National Synchrotron Radiation Laboratory, University of Science and Technology of China, Hefei, Anhui 230029, The People's Republic of China
[b] School of Nuclear Science and Technology, University of Science and Technology of China, Hefei, Anhui 230029, The People's Republic of China
[c] Hefei National Laboratory for Physical Sciences at Microscale, University of Science and Technology of China, Hefei, Anhui 230026, The People's Republic of China
[d] Xradia Inc., 5052 Commercial Circle, Concord, CA 94520, USA

ARTICLE INFO

Article history:
Received 2 August 2010
Received in revised form 7 September 2010
Accepted 20 September 2010
Available online 29 September 2010

Keywords:
Solid oxide fuel cell
Three-phase boundary length
X-ray computed nanotomography
Synchrotron radiation
Microstructure analysis

ABSTRACT

The visualization of three-dimensional (3D) microstructures of solid oxide fuel cells helps to understand the efficiency of the electrochemical conversion process, study the device's reliability, and improve manufacturing processes. Here, we used X-ray nanotomography to investigate a porous nickel–yttria-stabilized zirconia (Ni–YSZ) composite anode. These results were used to characterize and quantify the key structural parameters, such as the volume ratio of the three phases (Ni, YSZ, and pore), connected porosity, surface area of each phase, interface of Ni/YSZ, volume-specific three-phase boundary length (TPB where the Ni, YSZ and fuel gas phases come together), and electrical conductivity of the anode.

1. Introduction

Solid oxide fuel cells (SOFCs) have attracted much attention recently because of their high-energy conversion efficiency [1], environmental safety, and fuel flexibility. State-of-the-art SOFC electrodes are typically porous materials with complicated internal microstructures. Knowing their internal microstructures is critical for studying the relationship between the material properties and electrode performance. However, various technical challenges make it difficult to obtain 3D information about the manner in which regions are interconnected in internal space. Current analysis techniques, such as scanning electron microscopy (SEM) and transmission electron microscopy (TEM), can only provide two-dimensional (2D) or limited volume characterization of microstructures.

Recent advancements in microscopy techniques are contributing to the feasibility of gaining detailed 3D structural information of porous electrodes. A combination of focused ion beam (FIB) and SEM technologies has been used to study the 3D microstructures of SOFC materials, providing some important parameters such as three-phase boundary (TPB) length and gas-phase tortuosity [2–5]. Recently, FIB tomography techniques coupled with electrochemical simulation have also been used to analyze a solid oxide fuel cell anode [6].

X-ray computed nanotomography (nano-CT) is a widely available technique with many advantages. The best resolution ranges (20–50 nm) are available in many facilities [7–11], providing similar feature detectability to SEM. In addition to high spatial resolution, the penetrating power of X-rays enables imaging of large volumes. Moreover, the non-destructive nature of X-rays coupled with the operation of nano-CT in air allow for the possibility of in situ experiments. Therefore, nano-CT has been applied in many research areas such as nanomaterials, semiconductors, environmental sciences, and life sciences [8,10,12,13]. Izzo et al. used a nano-CT technique based on a lab source to image the 3D microstructure of a SOFC anode at a spatial resolution of 42.7 nm without physically removing the material, and then validated the results against direct-measurement techniques (e.g., mercury intrusion porosimitry) [14]. The lab-based nano-CT technique was corroborated by Shearing et al. with the combined FIB-SEM approach, demonstrating the precision of the nano-CT results over a large volume [15]. Recently, this approach has been extended to synchrotron radiation

* Corresponding author at: National Synchrotron Radiation Laboratory, University of Science and Technology of China, Hefei, Anhui 230029, The People's Republic of China. Tel.: +86 551 3601844; fax: +86 551 5141078.
** Corresponding author.
E-mail addresses: ychtian@ustc.edu.cn (Y. Tian), hqwang@ustc.edu.cn (H. Wang).
[1] These authors contributed equally to this work.

0378-7753/$ – see front matter © 2010 Elsevier B.V. All rights reserved.
doi:10.1016/j.jpowsour.2010.09.059

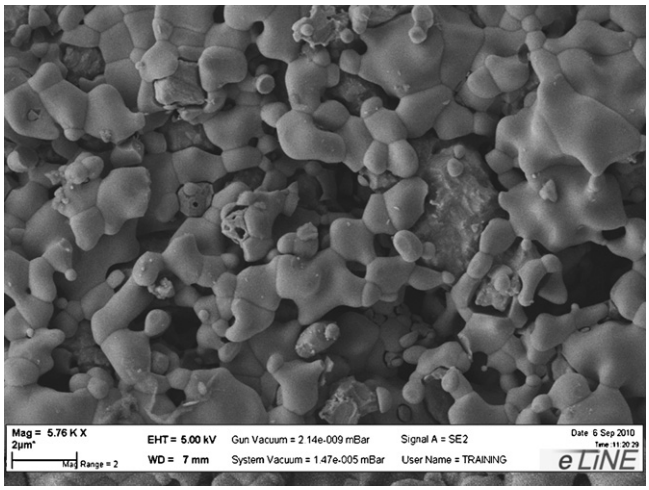

Fig. 1. The SEM of the Ni–YSZ anode.

and a tomographic imaging technique combined with numerical models to study the phase and pore networks of an SOFC anode [16].

2. Materials and experiments

In this study, the Ni–YSZ anode was chosen as the sample material. Coarse NiO (nickel carbonate decomposed at 600 °C, Sinopharm Chemical Reagent, China) and YSZ powders (BQ-8Y, Jiaozuo Weina Fine Ceramic, China) (NiO:YSZ = 56:44 wt.%) were used to fabricate the porous substrate supporting the anode by tape-casting processes. The anode was co-sintered at 1400 °C for 5 h, then heated to 800 °C and finally exposed to humidified H_2 (bubbled through water at room temperature) for 2 h. The surface morphology of the anode is shown in the SEM image (Fig. 1).

The nano-CT experiments were performed on the X-ray microscope beamline U7A of the National Synchrotron Radiation Laboratory (NSRL) in Hefei, China, using the Xradia nanoXCT-S100 system [17]. This XCT system achieves spatial resolution down to 50 nm with a total magnification factor of 880 onto the 1 k × 1 k Charge Coupled Device (CCD). A section of the sample SOFC material was polished to less than twenty microns and then glued to the top of a tungsten probe tip fixed into the sample holder, allowing full 180° rotation for CT image acquisition. A series of 181 radiographs was collected at angles ranging from −90° to +90° in 1° intervals and then reconstructed into a 3D volume using Xradia's reconstruction software [10]. In this study, 3D volume data acquisition by nano CT was carried out at two different locations of an anode, which are named sample 1 and sample 2.

Table 1
Sizes of two samples and voxel size.

	x	*y*	*z*
Sample 1			
Sample dimension (μm)	5.3	5.3	7.1
Sample 2			
Sample dimension (μm)	5.4	6.0	8.0
Voxel size (μm × μm × μm)	0.0583	0.0583	0.0583

3. Results and discussion

Using the absorption edge spectroscopic imaging technique, an element can be identified by differences in absorption intensities between the images taken above and below the absorption edge of the element under investigation [18]. Because of the tunable photon energy of the synchrotron source, two 3D scans were collected in absorption-contrast mode below (8300 eV) and above (8380 eV) the Ni K-shell absorption edge. Two radiographs of the sample 1 taken at 8300 eV and 8380 eV are shown in Fig. 2a and b, in which darker features represent regions of higher X-ray absorption. Because the contrast of Ni at 8380 eV was higher than at 8300 eV, it was possible to determine the absolute location of the Ni within the 3D matrix of the anode by comparing the difference between the reconstructed volumes from these radiographs. The other two phases could also be identified by comparison of the grey levels that did not change significantly over the 80-eV photon energy change.

Because the shape of the sample was irregular, two cuboids were cropped from the two reconstructed 3D volume data separately. The sizes of two reconstructed 3D volume and voxel size are summarized in Table 1.The volume data then were segmented into Ni, YSZ, and pore phases based on their grey levels. Fig. 3a shows one virtual slice from the cropped cuboid volume of sample 1, and Fig. 3b is the same virtual slice from the segmented volume. The processed 3D volume of sample 1 was rendered and is shown in Fig. 4 (Ni in red, YSZ in yellow, and pore space in blue). These results

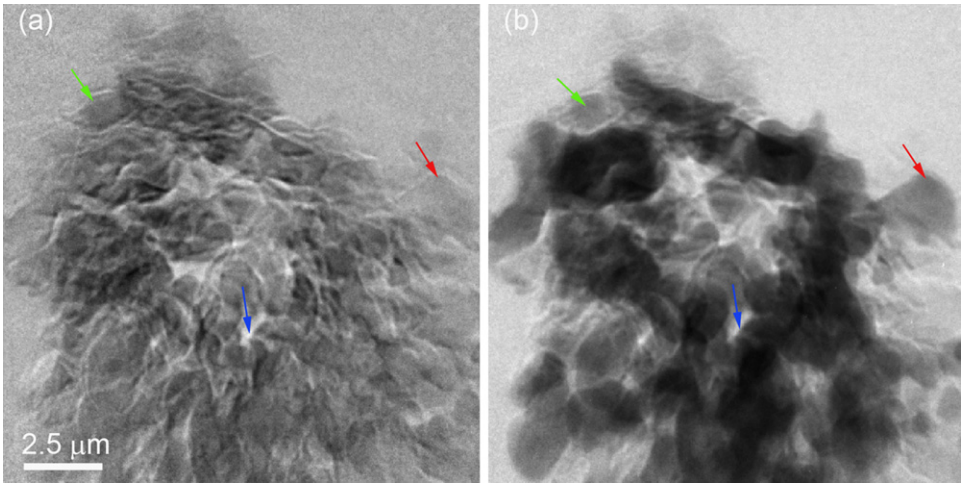

Fig. 2. 2D radiographs of the anode imaged (a) at 8300 eV (below the K-absorption edge of Ni) and (b) at 8380 eV (above the K-absorption edge of Ni). The darker pixels represent regions of higher X-ray absorption. The region with a strong contrast variation (red arrow) is the Ni phase; the region with a moderate grey level (green arrow) is the YSZ phase; and the brightest region (blue arrow) is the pore space. (For interpretation of the references to color in this figure legend, the reader is referred to the web version of the article.)

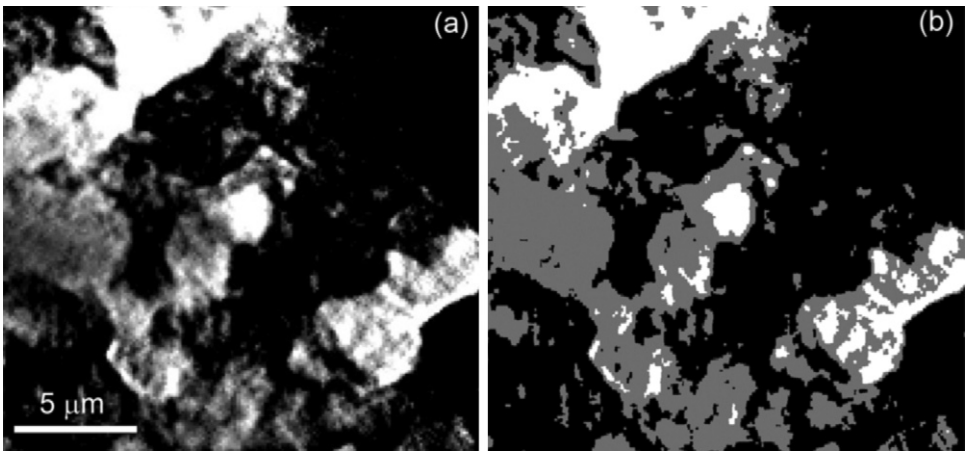

Fig. 3. (a) A virtual slice of sample 1, where white is the Ni phase, grey is the YSZ phase, and black is the pore space. (b) The same virtual slice after segmentation.

were subsequently used for quantitative analysis, as detailed in the following sections.

Below a certain volume size, the calculated porosity of the sample would fluctuate due to local structural effects and is not representative of the entire SOFC anode. To determine the minimum representative volume for analysis, an "expansion method" was developed. One vertex of the reconstructed volume was selected arbitrarily as the starting point. A number of sub-volumes that use the starting point as their common vertex were obtained by increasing the side length of the cube in x, y, and z directions. Simultaneously, the porosity of each cubical volume was calculated. Fig. 5 shows the cube size dependent of the calculated porosity of samples 1 and 2. The porosity fluctuations of both samples stabilized and the two curves coincided when the size of the cube was more than 4.6 μm (approximately 80 voxels). Thus, the two reconstructed volume could be representative of the whole anode.

The volume fraction of each phase was calculated by dividing the sum of the number of voxels assigned to that phase by the total image volume, and Table 2 shows the obtained results for the two samples. The initial volume ratio of NiO:YSZ powder in fabricating the anode was 56:44, which corresponded to the Ni:YSZ volume ratio of 40.6:59.4 after NiO was reduced to Ni. This Ni:YSZ volume ratio was very close to the calculated values from the 3D reconstruction of 39:61 and 40.3:59.7 for the two samples, demonstrating good agreement between the 3D-reconstruction-yielded results and the stoichiometry of the anode. This agreement not only indicated that the three phases were well distinguished but also validated image segmentation based on the spectroscopic study.

Connected porosity is the ratio of the connected pore volume to the total pore volume. We developed a method similar to the

Table 2
Summary of microstructural parameters measured from 3D reconstructions of samples 1 and 2.

	Sample 1	Sample 2
Volume fractions of Ni (%)	23.2	24.0
Volume fractions of YSZ (%)	35.8	35.6
Volume fractions of pore (%)	41.0	40.4
Surface area/volume of Ni (μm^{-1})	1.7	1.6
Surface area/volume of YSZ (μm^{-1})	4.1	3.9
Surface area/volume of pore (μm^{-1})	3.6	3.7
Interface area/volume of Ni/YSZ (μm^{-1})	1.2	0.9
Connected porosity (%)	40.7	40.0
Average Ni diameter (nm)	820	900
Average YSZ diameter (nm)	520	550
Average pore diameter (nm)	680	650
TPB length ($m\,cm^{-3}$)	4.44×10^6	3.10×10^6
Conductivity ($S\,cm^{-1}$)	188.99–502.74	233.10–597.07

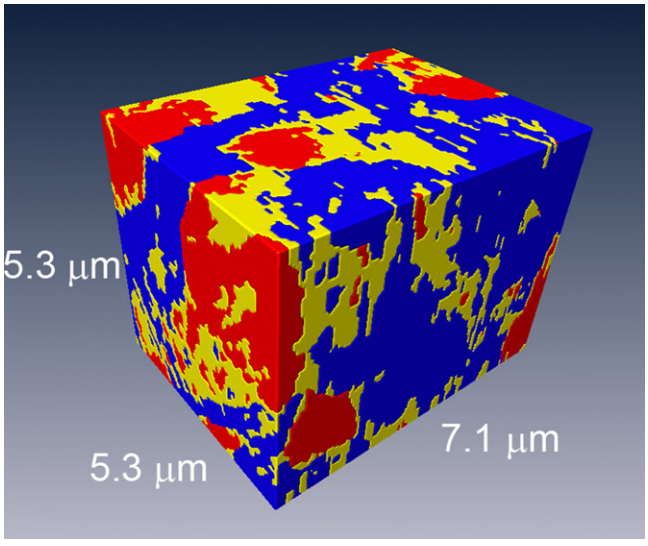

Fig. 4. A 3D rendering of sample 1, where Ni, YSZ and the pore phase are indicated in red, yellow, and blue, respectively. (For interpretation of the references to color in this figure legend, the reader is referred to the web version of the article.)

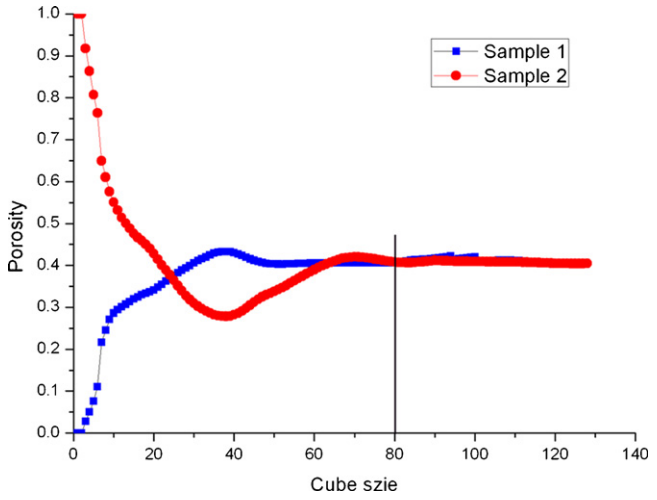

Fig. 5. Chart of the measured porosity of samples 1 and 2 as a function of the cube size. From these results, the minimum representative volume was determined to be ~80 voxels per size (~4.6 μm).

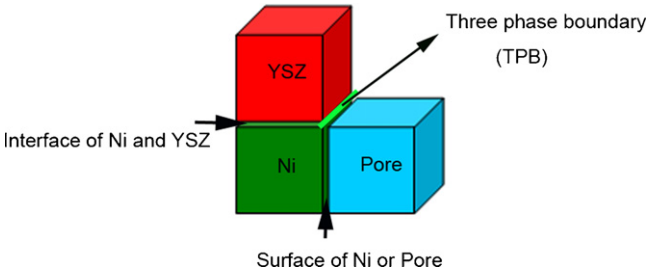

Fig. 6. Conceptual representation of the phase surface/interface and TPB. The cubes represent the voxels use for 3D reconstruction. The surfaces of the specific phases (such as Ni or pore) and the interface of Ni and YSZ are indicated. The TPB (green line) is the common edge of the three different elemental phases. (For interpretation of the references to color in this figure legend, the reader is referred to the web version of the article.)

"burning" method [19,20] to calculate the connected porosity. One side of the 3D volume was defined as the input end and the opposite side was defined as the output end. First, the pore voxels at the input end were chosen as the starting point. Any pore voxel that touched these voxels was set to the same label. From the input end to the output end, the labeled voxels formed a spanning cluster. From the output end to the input end, another spanning cluster was also formed with the same method. By comparing these two spanning clusters, the overlapped regions could be identified as the connected pores, whereas the rest were disconnected pores. Finally, the connected porosity was calculated by dividing the sum of the number of voxels assigned to the contiguous pore phase by the total pore volume. The connected porosity of samples 1 and 2 was calculated and listed in Table 2. Their difference was less than 2%, which demonstrated the validation of using the non destructive nano CT to analyze the electrode. The volume fractions of unconnected pores were 0.3% and 0.4% for samples 1 and 2, respectively. These unconnected pores are almost isolated in the 3D microstructure and thus do not contribute to gas transport. This information could be used to optimize the fabrication of the SOFC anode to improve the transportation of gas inside, which may improve the conversion efficiency.

Other parameters that can affect the anodic reaction, such as the surface area of each phase and the Ni/YSZ interface [21,22], were also obtained. Understanding the interface/surface area of each phase is helpful towards elucidating the electrochemical reaction mechanism and rate. First, three labels (Ni, YSZ, or pore) were assigned to the voxels in a 3D processed volume. As shown in Fig. 6, if a couple of neighboring voxels included two different labels, an interface of two phases or a surface of a specific phase was identified. By using a traversal method through the whole volume, the sum of the interface/surface could be achieved. As an approximation, each detected interface/surface contributed an area of about $58.3 \times 58.3\,nm^2$ to the interface/surface area. Therefore, the interface area of Ni and YSZ and the surface area of each phase can be exactly calculated. Table 2 summarizes the surface area/volume of each phase and Ni/YSZ interface area of both samples. Comparing the surface or interface area values of samples 1 and 2, the variation in the two sets of values was still within the acceptable range. These abovementioned quantitative data will be used latter to analyze the performance of the electrochemical reaction in the anode.

The Brunauer–Emmett–Teller (BET) formula $d = 6V/S$ [23,24] was utilized to calculate the particle/pore size, where d, V, and S are average size, volume and surface area, respectively. Table 2 shows the average diameters of Ni, YSZ and pore phase. Then the resolution of the system divided by the average diameters of three phases gave the expected errors of the particle sizes in each constituent, which were estimated to be 6.1%, 9.6% and 7.3% for the Ni, YSZ and pore phases of sample 1 and 5.5%, 9.0% and 7.7% of sample 2, respectively.

The electrochemical reaction only occurs at the TPB, and the electrochemical activity of Ni–YSZ anodes for the H_2 oxidation reaction is correlated to the TPB length [25]. The efficiency of the SOFC device improved with increasing TPB length, which can lead to the reduction of polarization losses [26,27]. A MATLAB program was developed at NSRL to quantitatively analyze the distribution of TPB and measure the TPB length of the anode. As presented above, if the neighboring four voxels in the labeled 3D volume had three different labels, the common edge of the three voxels was marked as TPB, as shown in Fig. 6. The TPB of the entire volume was obtained by applying this valuation separately to all virtual slices in the three directions x, y, and z. Fig. 7 shows the spatial distribution of TPBs of sample 1 and sample 2, which appeared to be asymmetrical within the analyzed sub-volume. According to the size of the voxel, the calculated volume-specific TPB length (vL_{tpb}) of the two samples in Table 2 were consistent with the evaluation of vL_{tpb} based on FIB-SEM tomography by Wilson et al. [5] and the results from model calculation by Janardhanan et al. [28].

Previous studies have shown that the volume fraction of the Ni phase can influence the value of the electrical conductivity, corresponding to a change in the electronic conduction mechanism through the metal phase [29]. In addition, a critical volume percent (percolation value) for the nickel phase leads to insulativity once the Ni content is under the percolation value. If the Ni content is too high, cermet structure instability may occur. Therefore, knowing the appropriate Ni content is essential for balancing the high electrical conductivity with the cermet structure stability. An expression based on the percolation theory developed by McLachlan can be used to roughly estimate the electrical conductivities of

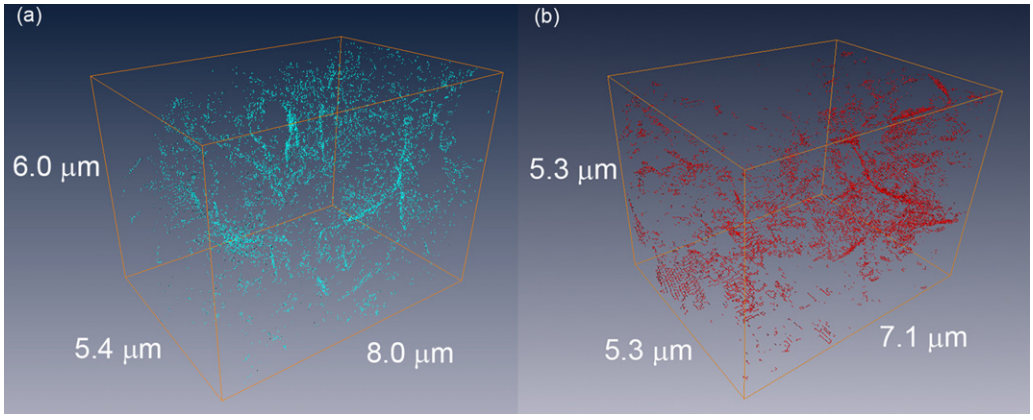

Fig. 7. The 3D distribution of the anode TPB. (a) The TPB of sample1. (b) The TPB of sample 2.

the composite [30,31].

$$\sigma_c = \sigma_{Ni}\left(\frac{V_{Ni} - V_c}{1 - V_c}\right)^t \quad (1)$$

where σ_c, σ_{Ni}, V_{Ni}, V_c, and t are the electrical conductivities of the composite and nickel phase, the volume percent and critical volume percent of nickel (with V_c and V_{Ni} expressed based on the entire composite volume), critical volume percent of nickel, and the conductivity exponent, respectively. The electrical conductivity of nickel (σ_{Ni}) is 25,700 S cm^{-1} at 800 °C [32], the critical volume percent of Ni is reported to be 16% [31], and the values of the conductivity critical exponents of the percolation system are considered to be universal ($t \approx 1.6$–2.0) in three-dimensional cases based on the renormalization group theory [33]. The V_{Ni} was the only parameter to be determined, which was measured from the 3D nano-CT anode data as V_{Ni} = 23.2% and 24% for samples 1 and 2, respectively. Combining all of the above data and using Eq. (1), the electrical conductivities of samples 1 and 2 were calculated (Table 2). It was found that the calculated electrical conductivities depended greatly on the Ni content. For validation of these results, we determined the electrical conductivity of the whole anode at 800 °C by four-electrode *I–V* measurement. This result indicated an electrical conductivity of 607.74 S cm^{-1}, which was close to the calculated result. These results demonstrated the potential of X-ray nanotomography to optimize the SOFC model by studying the relationship between the Ni volume fraction and the electrical performance of the SOFC anode.

4. Conclusion

The 3D microstructure of a SOFC anode was successfully characterized with X-ray nanotomography. Using an X-ray absorption spectroscopic technique, the 3D volume was segmented and then used to calculate several key parameters, such as volume fraction, surface area, three-phase boundary length, and electrical conductivity. These calculated parameters are critical for understanding the electrochemical conversion efficiency, studying the electrode reliability, and improving manufacturing processes.

At present, the major drawback of the X-ray nanotomography is that the whole electrode could not be imaged because of the limitation of imaging method; instead, different regions of the anode have to be selectively imaged to represent the entire electrode. Although it is proved that this method is viable, the large field of view (LFOV) technology is needed to study large enough regions of the electrode.

Acknowledgements

This work was supported by grants from the 985 project of the State Ministry of Education, the National Natural Science Foundation of China (No. 10734070), and the Knowledge Innovation Program of the Chinese Academy of Sciences (KJCX2-YW-N43).

References

[1] N.P. Brandon, S. Skinner, B.C.H. Steele, Annual Review of Materials Research 33 (2003) 183–213.
[2] T. Sakamoto, Z.H. Cheng, M. Takahashi, M. Owari, Y. Nihei, Japanese Journal of Applied Physics Part 1 – Regular Papers Short Notes & Review Papers 37 (1998) 2051–2056.
[3] D.N. Dunn, R. Hull, Applied Physics Letters 75 (1999) 3414–3416.
[4] R.K. Bansal, A. Kubis, R. Hull, J.M. Fitz-Gerald, Journal of Vacuum Science & Technology B 24 (2006) 554–561.
[5] J.R. Wilson, W. Kobsiriphat, R. Mendoza, H.Y. Chen, J.M. Hiller, D.J. Miller, K. Thornton, P.W. Voorhees, S.B. Adler, S.A. Barnett, Nature Materials 5 (2006) 541–544.
[6] P.R. Shearing, Q. Cai, J.I. Golbert, V. Yufit, C.S. Adjiman, N.P. Brandon, Journal of Power Sources 195 (2010) 4804–4810.
[7] J.L. Carrascosa, F.J. Chichon, E. Pereiro, M.J. Rodriguez, J.J. Fernandez, M. Esteban, S. Heim, P. Guttmann, G. Schneider, Journal of Structural Biology 168 (2009) 234–239.
[8] J. Chen, C.Y. Wu, J.P. Tian, W.J. Li, S.H. Yu, Y.C. Tian, Applied Physics Letters 92 (2008) 233104.
[9] Y.S. Chu, J.M. Yi, F. De Carlo, Q. Shen, W.K. Lee, H.J. Wu, C.L. Wang, J.Y. Wang, C.J. Liu, C.H. Wang, S.R. Wu, C.C. Chien, Y. Hwu, A. Tkachuk, W. Yun, M. Feser, K.S. Liang, C.S. Yang, J.H. Je, G. Margaritondo, Applied Physics Letters 92 (2008) 103119.
[10] A. Tkachuk, F. Duewer, H.T. Cui, M. Feser, S. Wang, W.B. Yun, Zeitschrift Fur Kristallographie 222 (2007) 650–655.
[11] W.J. Li, N. Wang, J. Chen, G. Liu, Z.Y. Pan, Y. Guan, Y.H. Yang, W.Q. Wu, J.P. Tian, S.Q. Wei, Z.Y. Wu, Y.C. Tian, L. Guo, Applied Physics Letters 95 (2009) 053108.
[12] C. Patty, B. Barnett, B. Mooney, A. Kahn, S. Levy, Y.J. Liu, P. Pianetta, J.C. Andrews, Environmental Science & Technology 43 (2009) 7397–7402.
[13] M.A. Le Gros, G. McDermott, C.A. Larabell, Current Opinion in Structural Biology 15 (2005) 593–600.
[14] J.R. Izzo, A.S. Joshi, K.N. Grew, W.K.S. Chiu, A. Tkachuk, S.H. Wang, W.B. Yun, Journal of the Electrochemical Society 155 (2008) B504–B508.
[15] P.R. Shearing, J. Gelb, N.P. Brandon, Journal of the European Ceramic Society 30 (2010) 1809–1814.
[16] K.N. Grew, Y.S. Chu, J. Yi, A.A. Peracchio, J.R. Izzo, Y. Hwu, F. De Carlo, W.K.S. Chiu, Journal of the Electrochemical Society 157 (2010) B783–B792.
[17] Y.C. Tian, W.J. Li, J. Chen, L.H. Liu, G. Liu, A. Tkachuk, J.P. Tian, Y. Xiong, J. Gelb, G. Hsu, W.B. Yun, Review of Scientific Instruments 79 (2008) 103708.
[18] K.G. Scheckel, R. Hamon, L. Jassogne, M. Rivers, E. Lombi, Plant Soil 290 (2007) 51–60.
[19] D.P. Bentz, E.J. Garboczi, Cement and Concrete Research 21 (1991) 325–344.
[20] D. Stauffer, Percolation Theory, Taylor and Francis, London, 1985.
[21] S.P. Jiang, S.P.S. Badwal, Journal of the Electrochemical Society 144 (1997) 3777–3784.
[22] S.P. Jiang, S.P.S. Badwal, Solid State Ionics 123 (1999) 209–224.
[23] L. Holzer, F. Indutnyi, P.H. Gasser, B. Munch, M. Wegmann, Journal of Microscopy-Oxford 216 (2004) 84–95.
[24] D. Gostovic, J.R. Smith, D.P. Kundinger, K.S. Jones, E.D. Wachsman, Electrochemical and Solid State Letters 10 (2007) B214–B217.
[25] R.J. Gorte, H. Kim, J.M. Vohs, Journal of Power Sources 106 (2002) 10–15.
[26] M. Mogensen, S. Skaarup, Solid State Ionics 86–8 (1996) 1151–1160.
[27] T. Fukui, K. Murata, S. Ohara, H. Abe, M. Naito, K. Nogi, Journal of Power Sources 125 (2004) 17–21.
[28] V.M. Janardhanan, V. Heuveline, O. Deutschmann, Journal of Power Sources 178 (2008) 368–372.
[29] N.Q. Minh, Journal of the American Ceramic Society 76 (1993) 563–588.
[30] R.M.C. Clemmer, S.F. Corbin, Solid State Ionics 166 (2004) 251–259.
[31] D.S. Mclachlan, M. Blaszkiewicz, R.E. Newnham, Journal of the American Ceramic Society 73 (1990) 2187–2203.
[32] M. Yousuf, P.C. Sahu, K.G. Rajan, Physical Review B 34 (11) (1986) 8086–8100.
[33] V.V. Novikov, D.Y. Zubkov, Physical Review B 73 (2006) 054202.